

The RADARSAT Geophysical Processor System

R. Kwok

Jet 1'70))//15/07/" D(loo?"/(/IT,(/"

California Institute of Technology

4800 Oak Grove Drive

Pasadena, CA 91109

1 Introduction

The RADARSAT Geophysical Processor System (RGPS) is a processing system dedicated to the analysis of Synthetic Aperture Radar (SAR) data of sea ice collected by the Canadian RADARSAT satellite [Raney *et al.*, 1991]. RADARSAT was launched in November of 1995 into a 24-day repeat cycle, an orbit configuration which provides near repeat coverage of the high latitudes at 3- and 7-day intervals. The SAR sensor has a number of imaging modes, one of which illuminates a wide swath (460 km) designed for large scale mapping of the Earth surface. The science plan of the Alaska SAR Facility calls for weekly coverage of the Arctic Ocean. With this mode, the coverage of the Arctic Ocean every seven days (Fig. 1) with 100 m pixels, produces approximately a gigabyte of image data daily. In an effort to make this large volume of SAR data more useful to the scientific community, the objective of the RGPS is to process this image data into fields of geophysical variables to a spatial and temporal scale suitable for supporting Arctic-scale science investigations.

A Geophysical Processor System (GPS) (Kwok and Baltzer, 1995) for processing of sea ice and ocean data was installed at the Alaska SAR Facility shortly after the launch of the European Earth Remote Sensing (ERS-1) satellite in July of 1991. During its three years of operation, this system had routinely provided products of ice motion and ice types. The GPS demonstrated the feasibility to produce geophysical products in a semi-automated fashion. The system filled part of the need to convert SAR images into geophysical data sets: it produced these products in roughly 100x100 km scene sized parcels. This system did not coalesce these data parcels into fields of observations, although some work by investigators moved in this direction. The narrow swath and limited data availability hampered some of these efforts. With the RADARSAT mapping mode and frequency of repeat coverage, it is

now possible to convert these high resolution radar datasets into large scale fields

The scientific goal of the RGPS is to provide datasets to improve our current understanding of the impact of sea ice on global climate. Interactions between sea-ice, ocean and atmosphere in the polar regions affect the Earth's climate. Sea ice growth, movement and decay affect energy and mass balance of the polar ocean system. The surface heat and brine fluxes associated with sea-ice growth contribute significantly to convection of the ocean and thermohaline circulation. Snow covered sea-ice reflects most of the incident solar radiation back into space, while fresh water fluxes associated with melting ice serve as stabilizing elements in the circulation of the North Atlantic waters. Processes along the ice margin and coastlines participate in water-mass formation, upwelling, convection sediment transport and other phenomena. Understanding and modelling these phenomena require information of sea-ice motion, thickness and concentration.

Five sea ice parameters are estimated and recorded in the RGPS system: ice motion, ice age/thickness, date melt onset/freeze-up, open water fraction and histograms of backscatter. Below, we describe the scientific relevance of these geophysical variables. A fundamental RGPS measurement is ice motion obtained by tracking common features in successive SAR images. In the RGPS, a Lagrangian view of the motion field is produced from a sequence of SAR imagery. From these observations, the ice age and ice thickness histograms of the thin ice fraction of the ice cover in the winter are derived. In the summer, we estimate the open water fraction from backscatter and area change information. The backscatter histogram of each cell recorded during each observation. The time of melt-onset in the spring and freeze-up in the late fall are estimated from changes in backscatter signature of the ice cover. These fields of geophysical variables will support process studies, model validation and the development of climatologies of sea ice processes.

Ice Motion. Large scale circulation of sea ice determines the advective part of the ice balance and provides a velocity boundary condition on the ocean surface. Smaller scale processes involve the detailed motion of individual floes, aggregate of floes and the formation of leads. Small scale ice motion controls the abundance of thin ice and thus the many surface processes dependent on thin ice, such as the heat flux to the atmosphere. Lead formation, during periods of divergent motion produce open water and thin ice areas that dominate the heat flux into the atmosphere and salt flux into the ocean. In contrast to this are pressure ridges that form during periods of ice convergence. Small scale motion and deformation of

the ice cover under wind and current stress are measurable in SAR data as has been demonstrated by numerous studies [Curlander *et al.*, 1985; Pily and Rothrock, 1987; Kwok *et al.*, 1990]. Time series SAR data provide a small scale view of sea ice motion.

Ice Age/thickness Distribution. The estimation of the thickness distribution is the primary motivation for tracking the ice age distribution. Among the many properties of sea ice strongly dependent upon its thickness are compressive strength, rate of growth, surface temperature, turbulent and radiative heat exchange with the atmosphere, salt content and brine flux into the oceanic mixed layer [Untersteiner, 1986]. Our present knowledge of the Arctic ice thickness distribution is derived largely from analysis of sonar data from submarine cruises. More recently, moorings with upward looking sonars have also been used to sample the thickness distribution at fixed locations. These and other remote sensing techniques under development for measurement of the ice thickness are reviewed in (Wadhams and Comiso, 1992; Thorndike *et al.*, 1992). These instruments typically provide a one dimensional transect of ice draft (or equivalently, thickness). The data are useful for computing the volume transport of ice through a region or building up a climatology of mean ice thickness over a long period of time.

The use of ice type as inferred from active [Kwok *et al.*, 1992] or passive microwave [Cavalieri *et al.*, 1984] datasets as a proxy thickness indicator of ice thickness, in substitution for the direct resolution of the thicker ice classes, is at best a poor replacement of direct measurement. Surface processes typically dominate the backscatter and emissivity observed by spaceborne sensors. At higher probing frequencies, atmospheric water vapor and cloud are additional confounding factors in the identification of ice types.

The age distribution of sea ice specifies the fractional area covered by ice in different age classes as a function of time. This age distribution is a fundamental quantity that can be measured using ice motion information by keeping track of the area changes of deforming cells [Kwok *et al.*, 1995]. In the Arctic Ocean in winter, new ice forms from freezing sea water that is exposed by the opening of leads in the ice cover. These horizontal openings manifest themselves as additions of areas to the local ice cover and are directly observable in time sequences of Synthetic Aperture Radar (SAR) imagery. The new ice in these leads ages and thickens. Repeated temporal sampling of these elemental areas provides us with an indication of when new areas or leads were created, the length of their existence, and thus a record of their age. The resolution of age is dependent on the sampling interval. With

some knowledge of the heat exchange between the atmosphere and ocean, the observed ice age distribution can be used to estimate the ice thickness distribution.

Melt Onset/Freeze Up. The location and timing of melt onset and freeze-up on Arctic sea ice play significant roles in a number of geophysical processes. A large decrease in surface albedo accompanies the onset of snow melt during the spring and thus increases the absorption and heating of the ice by the shortwave radiation. The rapid temperature decrease during freeze-up in the fall has an opposite effect on albedo and marks the beginning of the ice growth season and the end of the summer. The length of the melt season is defined by the two transitions described above. Changes in the timing and spatial patterns of these transitions and the length of the melt season are important parameters in polar climate and may also serve as sensitive indicators of climate change in the high latitudes.

Winebrenner et al. (1994) and Winebrenner et al. (1996) have shown that the onset of melt and freeze-up events are clearly detectable as changes in radar backscatter in ERS-1 imagery. During melt onset, the appearance of liquid water in the snow cover on multiyear ice is marked by a steep decrease (almost 9dB) in the observed backscatter. At the end of the summer, the backscatter from sea ice which survived the summer season increases rapidly as temperature falls below freezing and attains a stable backscatter which is characteristic of multiyear ice in the winter [*Kwok and Cunningham, 1994*].

Open Water Fraction. During the melt season, fresh water is reinjected into the upper ocean. Meltwater increases ocean stratification and therefore the heat flux between the ocean and atmosphere. The heat of the meltwater per ocean also increases as the total ice concentration decreases over the summer. The areal extent of open water is an important parameter to monitor for the understanding of the heat and mass balance of the ice cover.

After the onset of melt in the spring, the contrast between first-year and multiyear ice at C-band is lost and there is at present no effective means for ice type classification in the summer time. The sea ice cover at C-band has an average range of backscatter that is between -17dB and 12dB. At C-VV, open water backscatter is dependent on wind speed and is typically higher than that of the ice cover if the wind speed is above 4.5 m/s. The azimuthal look direction introduces only 1-2 dB of modulation of the backscatter at ERS-1 look angles. *Comiso and Kwok (1993)* use an algorithm which takes advantage of the higher backscatter of wind-roughened open water relative to the ice (Mel'nikov) to estimate the open water fraction. In addition to the large range of incidence angle in the RADARSAT

data, the SAR is operated at C-Band. For use in the RGPS, this algorithm is modified to take advantage of the higher backscatter of roughened water at near range and the lower backscatter of open water at the higher incidence angle at far range.

Time series of backscatter observations. The time-series evolution of backscatter contains information on the state of the surface of snow covered sea ice. It may be possible to link the conditions of the ice surface to a variety of energy and mass fluxes based upon the state of ablation of the snow and sea ice [Barber *et al.*, 1994]. The RGPS will collect time series histograms of backscatter within each Lagrangian cell to support investigations for relating the evolution of backscatter to geophysically relevant parameters.

The intent of this chapter is to provide a description of the RGPS, the processing algorithms and its data products. In the next section, we outline the algorithms which were implemented in the RGPS for analysis of the RADARSAT radar data. In section 3, the data products produced by the system are described. The implementation of the system is discussed in section 4. Summary remarks are provided in Section 5.

2 Sea Ice Algorithms

Ice motion and backscatter history are the primary measurements made directly from the time sequence of SAR imagery. The algorithms described herein are strongly dependent on the availability of this time series of ice motion and estimation of some of these geophysical variables would not be feasible without continuous observations of ice cover. The specific details of the algorithms described here can be found in the references in the text and elsewhere in this book and will not be given here. Rather, we use examples to illustrate the procedures.

2.1 Lagrangian Ice Motion

The ice motion tracker is based on the procedure described in Kwok *et al.* (1990). Briefly, the ice tracking algorithm operates on pairs of images separated in time by n -days, using a combination of area-matching and feature-matching techniques to track an array of points

from a source image to a target image. Initially, a regular array of points is defined on the first image of a series of images covering a region. These points constitute the corners of a regular array of square *cells* five kilometers on a side. The ice features at these points are identified and tracked in each of the subsequent images in the repeat observations using the ice tracking algorithm. This provides a set of ice displacement vectors. Fig. 2 shows the set of displacement vectors derived from ERS-1 imagery. Each point acquires its own trajectory, and the array of cells moves and deforms with the ice cover. The deformation of the ice cover as depicted using the trajectory information is shown in Fig. 3. This differs from the current GPS ice tracking strategy, in which the motion between image pairs is referred to an Earth-fixed grid, giving an Eulerian picture of the displacement field. The RGPS uses an ice tracker to follow the same set of points over a long time, giving a Lagrangian picture of the motion identical to that derived from drifting buoys.

2.2 Ice Age/Thickness

This procedure allows us to provide estimates of local age and thickness (distributions of the Arctic sea ice cover. We note that the algorithm works only during the winter and also that it provides a fine age resolution of only the young end of the age distribution. We refer to the time interval between sequential images as a time step. During each time step, the cell areas are computed. A positive change indicates that new ice was formed in the cell. A negative change is assumed to have ridged the youngest ice in the cell, reducing its area. The assumption here is that once ridging starts, the deformation tends to be localized in the thinner, weaker ice recently formed in the lead systems. The age classes are determined by the lengths of the time steps. The area of ice in each age class in each cell is updated at each time step. In this way, we keep track of the age distribution of the young ice.

The area of multiyear ice in each cell is also computed at each time step using the ice classification algorithm described in *Kwok et al.* (1992). The ice type algorithm uses a maximum likelihood classifier and a look-up table of expected backscatter characteristics to assign each image pixel to one of four classes: multiyear ice, deformed first year ice, undeformed first-year ice, and a low backscatter type characteristic of smooth, younger ice types and calm open water. Two possible sources of error are from wind-roughened open water and from frost flowers growing on new ice. Both of these physical phenomena exhibit highly variable radar backscatter, causing the classifier to label these pixels sometimes

incorrectly as multiyear ice. The time series of multiyear ice area for each cell is used to resolve these ambiguities, resulting in a more accurate classification. Since the area of multiyear (multiyear) ice within a cell should remain constant (because no multiyear ice is created in the winter), any anomaly which shows up as a transient spike or hump could be filtered out. The ice classification algorithm is not used to identify types of first-year ice because the accuracy of the classifier is lower for these ice types. Since the areas of young ice and multiyear ice in each cell are accounted for by the above procedures and the total cell area is known from its geometry, the residual area is simply labeled as first-year ice. For a series of five images with, say, three days between successive images, the age classes would be: 0-3 days, 3-6 days, 6-9 days, 9-12 days, first-year ice, and multiyear ice.

With records of the near surface air temperature, the young end of the age distribution is converted to a thickness distribution using a simple empirical relation between accumulated freezing-degree days and ice thickness (*Maykut, 1986*). We note that this scheme does not provide estimates of the thickness of first-year or multiyear ice. The present method provides a two dimensional, potentially basin-wide picture of the thickness of young ice, but it does not give any information about the mean thickness of the ice cover as a whole, since young ice occupies only a small fraction of the total area. The main output product of our age analysis procedure is the thickness distribution of young ice at a fine spatial resolution and the areal fraction of first-year and multi-year ice at regular time interval. Further details of how ice age is related to cell area changes can be found in *Kwok et al. (1995)*.

We select two examples to illustrate the procedure used for ice age computation within a cell. These cells are extracted from ERS-1 image sequences of the central Beaufort Sea acquired during 1992. The time series spans a period of 12 days from March 18 to March 30. The sampling interval or time step of the sequence is 3 days. The initial cell size is 5 km by 5 km. We assume, in the two examples shown here, that the initial distribution contains only first-year and multiyear in the cells. Table 1 and Figure 4 illustrate a few steps in the procedure. The increase in cell area, between Day 077 and Day 086, due to the continual opening of a lead, is evident. The area changes of the cell as a function of time are plotted in Figure 4b. This cell had an initial area of 2500 units, 1336 of which were classified as multiyear ice. Over the first time interval (Day 077 to Day 080), the area increased to 3034, giving a young ice class (which is between 0 and 3 days old), an area of 534 units. The remaining 1164 units were assigned to the first-year ice class of undetermined age. The cell area increased to 3205 and 3317 during the second (Day 080 and 083) and third (Day 083 and 086) time intervals,

respectively. This new area of 171 units created during the second time interval replaces the 534 units as the youngest age group. Similarly, the 112 units created during the third time interval replaces the 171 units as having the youngest age. The 534 units created during the first time interval have become 3-6 days and 6-9 days old, during the second and third time intervals, respectively. A closing event (between Day 086 and 089) caused a decrease in cell area from 3317 to 3235, or 82 units. At this time step, the newest age class has zero area since no new area was created, and the next youngest class loses $82 * \frac{k}{k-1}$ units to account for the lost cell area. The factor k accounts for the redistribution of thin ice into ridged ice, we assume that all ridged ice is k times its original thickness and occupies an area of $82 * \frac{1}{k-1}$. The area of this ridged ice is kept as a separate category in the age distribution record. Here, we use a value of $k = 5$ from the ridging study of Parmeter and Coon [1972]. Thus, approximately 20 units of ridged first-year ice is created from the an area decrease of 82 units. 1265 units were classified as multiyear ice, leaving 1235 units of old first-year ice. Note that the area of multiyear ice does not remain constant throughout the 12-day period. This is due to the high backscatter of the open lead, the signature of which overlaps with that of the multiyear ice backscatter, leading to an over estimation of multiyear ice. We discuss a procedure to resolve this classification error in the next section.

Table 2 shows the results from the temporal evolution of the grid cell in Figure 5. The grid cell is extracted from the image time-series. This cell increased in area during the first three time intervals, with a decrease in area during the last time interval in the sequence. The total decrease in area of $284 * \frac{k}{k-1}$ units during the last time interval is accounted for by decreasing the area of the three youngest age classes. 71 units of area are added to the ridged first-year ice category. The multiyear ice area remained relatively constant during the whole time sequence because the backscatter of the ice in the leads was low in this case.

The block diagram for the entire age/thickness scheme is shown in Figure 6. The measurements of ice displacements at each node and multiyear area within each cell are computed during each time step. The temperature at each cell is also recorded. The area changes of the CC11S are then used to update the age distributions as described above. The thickness distribution is then determined using the temperature record accumulated for that cell. Some features of the scheme are described below.

The age distribution needs to be initialized at fall freeze-up. Since we do not know the ice age distribution at freeze-up, observations must be made for a period of time before the initial

conditions or initial age distribution no longer affect the age distribution estimates. This start-up period is determined by the oldest age class (excluding first-year and multiyear) we decide to track. For example, if the oldest desired age class is 30 days, then it will take 30 days for the initial conditions (young ice present at start-up) to grow into the first-year category. Or, the initial distribution of ice in the 0-30 range would have 'aged' beyond the range of observation. After this period, the initial conditions are determined and the age distribution will be correctly represented with the computational procedure above.

As previously noted, the presence of wind-blown open water or frost flowers on thinner ice could cause the ice classifier to over-estimate the area of multiyear ice even though the winter signature of multiyear ice has been shown to be stable [Kwok and Cunningham, 1994]. Using the time series of multiyear ice for a particular cell these mis-classification events can be identified as positive spikes or humps. Filtering out these events leaves the 'background' or true multiyear ice area. This may still not be perfectly constant since the cell boundaries (straight lines connecting the corner nodes) are not necessarily material boundaries and these moving edges can cause ice to shift into or out of a cell. We use a simple procedure to estimate the average multiyear ice area [Kwok *et al.*, 1995]. Figure 6 shows observed multiyear ice area for the two grid cell examples used in the previous section; the dashed line indicates the estimated multiyear ice area determined with this procedure. In the first example, the newly-opened lead has a backscatter signature which overlaps with that of multiyear ice and therefore increased the estimated areal fraction of multiyear ice in the grid cell. As the ice in the lead aged, its backscatter evolved toward a more first-year ice-like signature and appearance, resulting in a decrease in area of multiyear ice. The multiyear ice area returned to approximately its area before the lead opened. The second example shows that the backscatter of the ice in the leads remained low and therefore did not confound the backscatter-based classifier. In both cases, a reasonable estimate of the multiyear ice fraction was obtained.

It is the freezing rate, not temperature or time alone, that tells the thermal history of each age class. To convert age to ice thickness, we must know the freezing rate. We approximate this rate as being proportional to the number of freezing-degree days (*FDD*) associated with each age class of each cell. In Table 1, we have recorded the mean temperature, over each time interval. It is obvious that the accuracy of the temperature field is important, we discuss the source of the temperature fields we use in the RGPS in the next section. We convert the age distribution, to thickness distribution, with a simple procedure which

utilizes the dependence of thickness, H , on freezing-degree days, F . For each area of young ice, there is an upper and lower bounds on the age of the ice due to the length of each time step: the opening in the ice could be created during the beginning or near the end of the time step. Consequently there are two values of F , F_{upper} and F_{lower} , that apply to each age category. We do not keep track of F for the first-year and multiyear classes. We used Lebedev's parameterization (discussed in *Maykut*, 1986), with $F = 1.33 H^{0.58}$. This relationship is based on 24 station years of observations from various locations in the Soviet Arctic. Lebedev's parameterization describes ice growth under "average" snow conditions, in contrast to others which describes ice growth with little or no snow cover. The thickness of the snow cover is an important parameter which controls ice growth, but there is at present no routine measurements of snow depth over the ice cover.

The F_{upper} and F_{lower} bounds of ice thickness for each age class are shown in Figures 4c and 5c. The high rate of ice growth when the ice is young gives the largest uncertainty in the thickness in this youngest age class. This uncertainty improves as the ice ages and the growth rate decreases. The area occupied by sea ice within a thickness range can be read directly from the Figs. 4c and 5c. Certainly, a more sophisticated model could be implemented for computation of ice thickness, and this could easily be incorporated at a later stage. Fig. 8 shows a snapshot of the thin ice fraction computed from the trajectories used to create Fig. 3.

2.3 Summer Open Water Fraction

The summer open water fraction within each cell is determined with an algorithm which uses the wind dependent characteristics of open water. We first compute the expected backscatter cross-section of open water using the surface wind speed and its direction relative to the radar look direction at each point. A C-HH model function (constructed from current C-VV model functions using the expected co-polarized response of open water) is used to provide the backscatter cross-section of HH using the above information. Sea ice (bare ice, ice with wet snow cover) has a very narrow range of backscatter, between -17 dB and -12 dB. At C-HH, depending on the wind velocity and incidence angle, the backscatter of HH water could be above or below that of the ice. We do not estimate the open water fraction if the backscatter of water and ice overlap. At points where the open water backscatter is above or below that of the ice, we use backscatter thresholds computed using

the model function to determine whether a pixel belongs to the open water category. Fig. 9 shows an ice/open water ERS-1 and the corresponding classification map of water and ice. The C-VV model function is used in this case.

2.4 Melt Onset/Freeze Up

The backscattering cross section of a Lagrangian cell is recorded at each time step. A time series of backscattering cross section histogram of each cell is used to determine the date of melt onset and freeze-up. The melt onset algorithm tracks the peak of the histogram for cells with more than $M\%$ multiyear ice. The detection criterion is when the peak value dips below a predetermined threshold. We estimate the date to be the time when the temporally interpolated peak crosses this threshold. The freeze-up algorithm also tracks the peak of the backscattering histogram. When this peak remains above a specified threshold for a period of N days, estimate M days prior to the threshold crossing to be the date of freeze. The details and basis for these algorithms are discussed in Chapter xx.

3 RGPS Products

The measurements made at each time step are stored in three main tables (Table 3): the connectivity table, grid point trajectory table and the cell attributes table. This information is available to users who need the tables at the lowest level. The size of these tables grow linearly with time. There are a total of fourteen RGPS products (Table 4) derived from these tables. Seven products are produced directly from the Lagrangian ice motion observations; they contain information and properties about individual cells. Six gridded products (50 km grid), on an SSM/I polar stereographic projection, are summary products derived from the cell dataset. The last product contains gridded sea level pressure, surface wind and temperature estimates which were used in the analysis of the SAR data.

3.1 Database Tables

Grid point trajectory Table. At each time step, the geographic location of that grid point is recorded. This table is updated each time a grid point is tracked to a new location.

Connectivity Table. This keeps track of the number of points in the polygon used to define a cell. For each cell, the grid point identifiers of the vertices of the polygon are stored. Also, the birth and death dates of the cell are stored. This table is updated when a grid point or cell is added or deleted. For example when a grid point is deleted, the cells which are defined by that grid point are no longer valid and thus causes the death of these cells.

Cell Attributes Table. The properties of each cell e. g. backscatter histogram, multiyear ice fraction, area, etc. are stored in this table which is updated at each time step

3.2 Products

Ice Motion (Lagrangian/Eulerian). Operationally, a regular array of points is defined initially on the first image of a long time series of SAR images and the ice motion tracker finds the positions of those points in all subsequent images of the series. This Lagrangian product contains a record of the trajectories or an array of position measurements of the 'ice particles' that are located on the initial grid which covers a region or the entire Arctic Ocean. The sampling interval is determined by repeat coverage of these points by SAR imagery. With an initial grid spacing of 5 km, there are approximately 500,000 points in this array. Over a winter season of approximately eight months, there are close to 32 observations for each trajectory. The gridded 50 km Eulerian product represents weekly ice motion which are optimally interpolated to the grid locations from these trajectories. We produce routine Eulerian observations of ice motion from image pairs for locations like the Greenland Sea and South of the Bering Strait, where the character of the ice motion is such that the deformation does not allow us to maintain the density of points to define a Lagrangian grid. In these special regions, we select a high repeat coverage frequency.

Ice Age Histogram. The ice age distribution of sea ice specifies the fractional area covered by ice in different age classes, within a given region, as a function of time. This ice age distribution is computed from the field of Lagrangian trajectories described above. The

algorithm for determining ice age works only in the winter: the assumption is that there is ice growth in all new leads. The process for ice age determination is initialized shortly after fall freeze-up and is operated till the onset of melt. For each observation of a cell, we update the ice age histogram. The resolution of age is dependent on the sampling interval of the area of interest. As an example, for a series of images with, say, seven days between successive images, the age classes would be: 0-7 days, 7-14 days, 14-21 days, 21-28 days, ..., first-year ice, multiyear ice and ridged first-year ice. We note that the ice age categories for a given age histogram do not necessarily have the age ranges because the sampling intervals could be non-uniform. The multiyear ice fraction is obtained using an ice classification algorithm. The accumulated freezing-degree days associated with each age class is also recorded. The surface air temperatures for computing the freezing-degree days are extracted from analyzed temperature fields (described below). There are three ice age histogram products. The first ice age histogram product contains records of local ice age distributions and the accumulated freezing-degree days of each age class within each Lagrangian cell. The interpolated ice age histogram product provides uniform age categories (3-day) rather than the non-uniform age categories in the previous product. The last product is a gridded (50km) product which summarizes the ice age histograms on an Earth fixed grid.

Ice Thickness Histogram The ice thickness distribution specifies the fractional area covered by ice in given thickness ranges within a region as a function of time. The ice thickness distribution is estimated from the ice age distribution using an empirical relationship between freezing-degree days and ice thickness as described above. The highest resolution products provide the ice thickness histograms of the Lagrangian cells. Again, a 50 km gridded product of the ice thickness histograms is produced from the cd1 observations.

Open Water Fraction. Summer ice conditions will be characterized by an open water fraction product. The summer open water fraction in a Lagrangian cell is estimated from kinematics and backscatter data. Kinematics gives the expected area change relative to a previous observation and the backscatter distribution provides an estimate of the areal coverage of open water in a cell.

Backscatter Histogram of Lagrangian cells. The backscatter histograms of the Lagrangian cells are recorded in this product. The backscatter histogram for each cell is saved in twenty 1 dB bins. The backscatter history will allow the correlation of surface properties of the sea ice to atmospheric and surface conditions.

Date of Melt-onset in Spring/ Freeze-up in Fall. There is a fairly well-defined change in the backscatter of the snow/ice to the onset of melt and freeze-up. The analysis algorithm will detect and estimate the date this seasonal transition using the time series of backscatter product. Different parts of the Arctic go through these transitions at different dates and this product would provide a high spatial resolution of the date of transition although the temporal resolution is dependent on the repeat observations of the Lagrangian cells.

Daily Gridded Fields of Pressure, Temperature and Geostrophic Wind. The gridded surface pressure and wind fields are derived by interpolation of the pressure and wind fields from obtained from the National Meteorological Center (NMC). The analyzed temperature field is a 6-hourly, 2-m temperature data set [Martin and Munoz,1996] provided by the POLS (POLar Exchange at the Sea Surface), a NASA interdisciplinary project. The gridded air temperatures are estimated using an optimal interpolation scheme with temperature inputs from drifting buoys, manned drifting stations, coastal land weather stations and ship reports. These are the air temperature estimates we use in the conversion of ice age to ice thickness.

3.3 Sampling Issues and Measurement Errors

Spatial and Temporal Undersampling. The spatial sampling of the small scale motion field is limited by the density of grid points. In this case, the spatial sampling of the motion field is on the order of 5 km, thus smaller scale motion details are not resolved and the field is undersampled. The deformation of a region of ice is represented by these deforming polygons, so the geometry of the region is very coarsely represented. We do not know the quantitative effect of this spatial undersampling. The motion field is also temporally undersampled. The sampling rate is dependent on the repeat observation of a region which in our case is constrained by orbit geometry and repeat cycles. Again, the motion details between observations are not resolved and the temporal record is undersampled. The temporal undersampling has a direct effect on the computation of total open water production and ridging. These parameters will be underestimated as was suggested by Fowler *et al.* (1996). Coon *et al.*(1996) studied the effects of undersampling using buoy data and suggested correction factors to compensate for the weekly sampling issue.

Measurement Errors. These are two primary sources of error in measuring ice motion from satellite imagery: (1) the geolocation uncertainty of each image pixel; and (2) the tracking

error which is the uncertainty in identifying common features in an image pair. A more detailed discussion of these errors can be found in *Holt et al.* (1992). For ERS-1 imagery, the uncertainty in ice displacement is approximately 0.3 km. Deformation computations are typically not affected by geolocation errors if these errors are positional biases. For SAR imagery, the geolocation errors are biases and the variations are negligible within an image. *Stern et al.* (1995) estimated that uncertainty in divergence computed from the GPS ice motion products is approximately 0.008. For RADARSAT, these errors need to be re-assessed.

4 The System

The mapping approach uses the RADARSAT ScanSAR Wide B mode to provide a close to 7-day repeat coverage of the Arctic Ocean and adjacent Seas. The swath width of this mode is approximately 460 km. The drift of the orbit over seven days, within the 24 day repeat cycle, is modest and always eastward. In our approach, the passes from days 3 and 4 are used for the first map (Fig. 1). This mapping is completed in 48 hrs. Later maps are made on days 10/11, 17/18 and 24/1. Each map takes less than 107 mins of radar-on time. In the following 24-day cycle, we repeat the mapping starting with passes from days 3 and 4. The interval in days between the maps are 3,7,7 and 7. This sequence is repeated for all cycles. The maps are constructed predominantly with descending passes and gaps are filled with ascending passes. Over a 24-day repeat period, 423 mins of ScanSAR data are required to map the Arctic Ocean for the purposes of the RGPS. This represents a daily data rate of close to fourteen 500 Km x 460 Km ScanSAR images.

Throughput/Storage. The RGPS throughput is designed to slightly exceed this daily rate to accomodate a certain amount of reprocessing of the data. The computation capability required to sustain this throughput is provided by application accelerators which provide an aggregate floating point performance of approximately 1 Gflops. We store approximately 30 days of image data in the system for efficient pairing of the image frames for motion tracking. In addition, storage space is required to accomodate the database tables described in the previous section. A total storage capacity of 100 GB is available for such purposes.

Ice Motion Tracking. The Lagrangian observations are sensitive to errors introduced by the tracker because errors in location propagate through the time sequence. In the RGPS, all results from the automated tracking procedure are visually inspected by an operator before the observations are recorded. To make this process more efficient the operator is provided with the capability to view areas of large deformation as designated by the tracker and to correct the tracker results where appropriate.

Other Data Sources. The system assimilates data wind and pressure data produced by the National Meteorological Center (NMC) and re-grids them into a Polar Stereographic projection. Also, the 2-m temperature field (described previously) is provided to us by the POLES project. These datasets are used in the analysis of the SAR data.

Archive and Distribution. The RGPS does not archive and distribute data products. The RGPS products are delivered to the Alaska SAR Facility where they are archived and distributed to users.

Flexibility. A goal in system development is to provide the flexibility for ease of incorporation of new algorithms. We envisage that new algorithms and methods to enhance current algorithms will be proposed as the science community develops experience working with SAR data and the current set of geophysical products. The system is designed such that the addition of new algorithms are a relatively simple procedure.

5 Summary and Discussion

We have described the sea ice algorithms that are used to generate the RGPS data products. The processing system described here serves three purposes: (1) To transform values of radar backscatter into fields of information that are **11 S(1'111** for scientists; (2) To analyze images consistently, so that comparisons can be made over wide spatial and temporal scales without bias due to processing; and (3) To handle large volumes of data. The RGPS algorithms give us an opportunity to estimate sea ice parameters (ice age/thickness) previously inaccessible using other datasets. The potential payoffs in geophysical understanding of the polar regions will be very large if the radar coverage and data quality allow us to routinely make basin-scale observations of the Arctic Ocean.

In April of 1994, an RGPS Working Group was established to define the geophysical variables which could be routinely extracted from the RADARSAT SAR data, to specify the data products and to monitor the implementation process and the evolution of the system. The current membership contributes directly to the development of the analysis algorithms and definition of the data products. This group is also responsible for the verification of the system, the validation of the data products and processing strategy. We define verification as the process used to confirm that the system and procedures work as designed and validation to be the test of scientific validity of the products. After the initial release of RGPS data products, we envisage a larger group which includes participation of the broader user community to facilitate exchange of information and ideas amongst users of the products.

At the time of this writing (June 1996), the RADARSAT commissioning phase activities are drawing to a close. These activities include the checkout of the space segment, ground segment and the calibration of the RADARSAT beams. The release of the SAR data for RGPS analysis will be available shortly. Based on the current schedule, the implementation of RGPS will be completed in October of 1996. This is followed by a six-month verification phase, for assessment of the performance of the system and the verification of the algorithms, after which the system will start routine processing of the Arctic Ocean data.

Acknowledgments

R. Kwok performed this work at the Jet Propulsion Laboratory, California Institute of Technology under contract with the National Aeronautics and Space Administration.

References

- Barber, D. G., T. I. Papakyriakou and E. F. LeDrew, 1994, The relationship between energy fluxes, dielectric properties, and microwave scattering over snow covered first year ice during the spring transition period, *J. Geophys. Res.*, **99**(C11), 22401-22411, 1994.
- Cavalieri, D. J., P. Gloersen and W. J. Campbell, Determination of sea ice parameters from Nimbus 7 SMMR, *J. Geophys. Res.*, **89**(D4), 5355-5369, 1984.
- Coon, M. D., G. S. Knoke and D. C. Echert, Compensating for daily lead-width motion when calculating open-water production from weekly data. NWRA Report. NWRA-CR-96-R158.
- Curlander, J. C., B. Holt, K. C. Hussey, 1985, Determination of sea ice motion using digital SAR imagery, *IEEE J. of Oceanic Engineering*, **OE-10**(4), 368-377, 1985.
- Fily, M. and D. A. Rothrock, Sea ice tracking by nested correlations, *IEEE Trans. Geosci. Remote Sens.*, **GE-25**(5), pp. 570-580, 1987.
- Fowler, C., W. Emery and J. Maslanik, The Consequences of 7-day Sampling for RADARSAT Ice Motions and 1-Derived Fields, 1995.
- Holt, B., D. A. Rothrock and R. Kwok, Determination of sea ice motion from satellite imagery, in *Microwave Remote Sensing of Sea Ice*, Ed. F. D. Carsey, Geophysical Monograph 68, AGU, 1992.
- Kwok, R. and C. Baltzer, The Geophysical Processor System at the Alaska SAR Facility 1995, *Engng. and Remote Sens.*, **vol. 1**, No. 12, 1445-1453, 1995.
- Kwok, R., D. A. Rothrock, H. Stern and G. F. Cunningham, 1995, Determination of Ice Age using Lagrangian Observations of Ice Motion, *IEEE Trans. Geosci. Remote Sens.*, **vol. 33**, No. 2, pp. 392-400, 1995.
- Kwok, R. and G. Cunningham, Backscatter Characteristics of The Sea Ice Cover in the Winter Beaufort Sea, *J. Geophys. Res.*, **99**(C4), 7787-7802, 1994.
- Kwok, R., E. Rignot, B. Holt and R. G. Onstott, Identification of Sea Ice Types in Spaceborne SAR Data, *J. Geophys. Res.*, **97**(C2), 2391-2402, 1992.

- Kwok, R., J.C. Curlander, R. McConnell and S. Pang, An Ice Motion Tracking System at the Alaska SAR Facility, *IEEE J. of Oceanic Engineering*, Vol. 15, No. 1, 44-54, 1990.
- Martin, S. and E. A. Munoz, Properties of the Arctic 2-m air temperature for 1979-present derived from a new gridded data set, *J. Climate*, (submitted), 1996.
- Maykut, G. A., The Surface Heat and Mass Balance, in *Geophysics of Sea Ice*, Ed. N. Untersteiner, Series B: Physics Vol. 146, Plenum Press, 1986, p. 423.
- Parmeter, R. R. and M. Coon, Model of pressure ridge formation in sea ice, *J. Geophys. Res.*, , 77, 6565-6575, 1972.
- Raney, R. K., A. P. Lascombe, E. J. Langham and S. Ahmed, RADARSAT, *Proceedings of the IEEE*, Vol.79, No. 6, June, 1991.
- Stern, H. I., D. A. Rothrock and R. Kwok, Open Water Production in Arctic Sea Ice: Satellite measurements and model parameterizations, *J. Geophys. Res.*, 100 (C10), 20601-20612, 1995.
- Thorndike, A. S., C. Parkinson, D. A. Rothrock, Editors, *Report of the Sea Ice Thickness Workshop*, 19-21 November 1991, New Carrollton, MD, Applied Physics Laboratory, University of Washington, 1992.
- Untersteiner, N., Ed., *The Geophysics of Sea Ice*, Series B: Physics Vol. 146, Plenum Press, 1986.
- Wadhams, D. and J. Comiso, The Ice Thickness Distribution Inferred Using Remote Sensing Techniques, in *Microwave Remote Sensing of Sea Ice*, Ed. F. D. Carsey, Geophysical Monograph 68, AGU, 1992.
- Winebrenner, D. P., E. D. Nelson, R. Colony, R. D. West, Observations of melt onset on multiyear Arctic sea ice using ERS-1 synthetic aperture radar, *J. Geophys. Res.*, , 99(C11), pp. 22421-22441, 1994.
- Winebrenner, D. P., B. Holt, E. D. Nelson, Observation of autumn freeze-up in the Beaufort and Chukchi Seas using ERS-1 synthetic aperture radar, *J. Geophys. Res.*, , in press.

Table 1

Record of Parameters (Area changes, Age Distribution) from Time-sequence Analysis
(Example 1)

Record	Time (DAY:HH)	Mean Temp, T	Cell Area, A^*	FDD	Area* of Age Class j							MY	Ridged FY
					1	2	3	4	1 %				
1	077:22	-23	2500						11.64			1336	0
2	080:22	-20	3034	65	534				598			1902	0
3	083:22	-20	3205	126	171	534			536			1964	0
4	086:22	-19	3317	166	112	171	534		1046			1454	0
5	089:22	-17	3235	229	0	10	171	534	12.35			1265	20

* 1 pixel = $100m \times 100m = 10000 m^2$ = unit area

FDD = Cumulative freezing-degree days

Table 2

Record of Parameters (Area changes, Age Distribution) from Time-sequence Analysis
(Example 2)

Record	Time (DAY:HH)	Mean Temp, T	Cell Area, A^*	FDD	Area* of Age Class j							MY	Ridged FY
					1	2	3	4	1 %				
1	077:22	-23	2000						692			1808	0
2	080:22	-20	2736	65	236				575			1925	0
3	083:22	-20	2807	126	71	236			612			1888	0
4	086:22	-19	2981	166	112	71	236		5.40			1960	0
5	089:22	-17	2697	229	0	0	0	126	588			1912	71

* 1 pixel = $100m \times 100m = 10000 m^2$ = unit area

FDD = Cumulative freezing-degree days

Table 3

RGPS Database Tables

Grid Point Trajectories

Grid point identifier 1	Time of observation
	Latitude
	Longitude
Grid point identifier 2	Time of observation

Grid Connectivity Table

Cell identifier 1	Number of Vertices (N)
	Grid point identifier 1
	Grid point identifier N
	Birth Date
	Death Date
Cell identifier 2	Number of Vertices (N)

Cell Attributes Table

Cell identifier 1	Time of observation
	Area
	Air Temperature
	Wind u, v
	Winter: multiyear ice area
	Summer: open water fraction
	Incidence angle
	Backscatter histogram
Cell identifier 2	Time of observation

Table 4

RGPS Data Products

Description	Season	Grid Spacing	Frequency
Lagrangian motion trajectories	Winter/Summer	Variable	Weekly
Gridded ice motion	Winter/Summer	50 km	Weekly
Eulerian ice motion	Winter/summer	5 km	Variable
Ice age histogram	Winter	Variable	Weekly
Ice age histogram (interpolated)	Winter	Variable	Weekly
Gridded ice age histogram	Winter	50 km	Weekly
Ice Thickness histogram	Winter	Variable	Weekly
Gridded ice thickness histogram	Winter	50 km	Weekly
Area/open water fraction	Summer	Variable	Weekly
Gridded open water fraction	Summer	50 km	Weekly
Backscatter histogram	Winter/Summer	Variable	Weekly
Gridded backscatter histogram	Winter/Summer	50 km	Weekly
Melt Onset/Freeze Up	Winter/Summer	Variable	Twice yearly
Gridded Wind/Temp/Pressure	Winter/Summer	50 km	Daily

Figure Captions

Figure 1.1. ADARSAT Snapshot of the Arctic Ocean using ScanSAR coverage from Days 3 and 4 of the repeat cycle.

Figure 2. Displacement vectors (arrows) derived from a pair of ERS-1 SAR images (ERS1 images: (c) ESA 1996).

Figure 3. Deformation of the ice cover (May 92 thru July 1993) constructed from Lagrangian ice motion observations. A simulation. (The Lagrangian trajectories are created from AVHRR ice motion observations).

Figure 4. Determination of ice age distribution and thickness distribution in a grid cell extracted from the time sequence (Example 1). (a) The image sequence showing the deformation of a grid cell. (b) Plot of area changes as a function of time, and age histograms computed from the area changes. (c) Plot of the freezing-degree days and the computed thickness of the ice. (* 1 pixel = $100m \times 100m = 10000 m^2$ = unit area) (ERS1 images: (c) ESA 1996)

Figure 5. Determination of ice age distribution and thickness distribution in a grid cell extracted from the time sequence (Example 2). (a) The image sequence showing the deformation of a grid cell. (b) Plot of area changes as a function of time, and age histograms computed from the area changes. (c) Plot of the freezing-degree days and the computed thickness of the ice, (* 1 pixel = $100m \times 100m = 10000 m^2$ = unit area) (ERS1 images: (c) ESA 1996)

Figure 6. Block diagram showing the general scheme.

Figure 7. Plot of the area of MY ice, $B_{k,MY}$, in the two grid cells. (a) Grid cell 1; (b) Grid cell 2. Dashed line shows the average MY area, A_{MY} , computed using the procedure in the text. (* 1 pixel = $100m \times 100m = 10000 m^2$ = unit area)

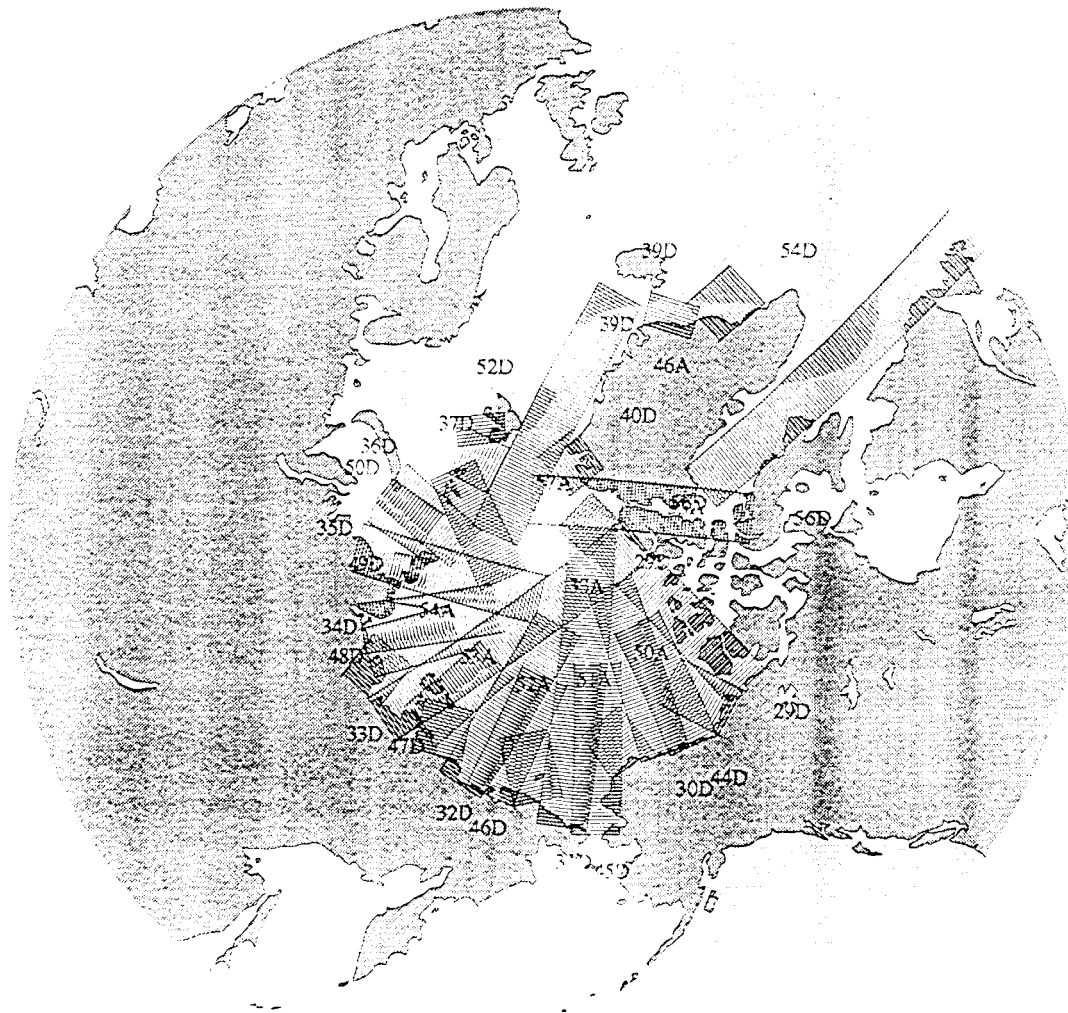
Figure 8. Thin ice fraction (< 25 cm) estimated by the ice age/thickness algorithm using the simulated ice motion trajectories used to create Fig. 3.

Figure 9. Open water fraction computed using the expected backscatter of wind roughened

water as threshold. (ERSI images:©ESA 1996)

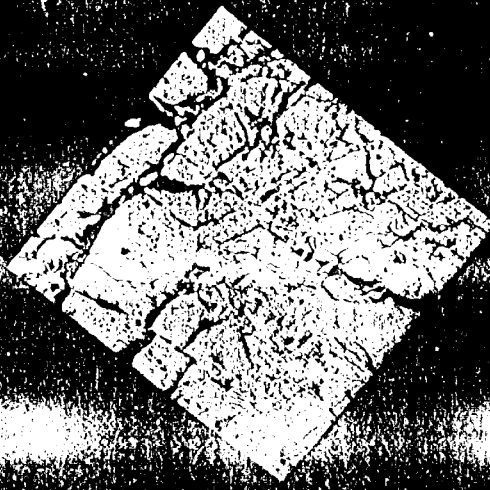
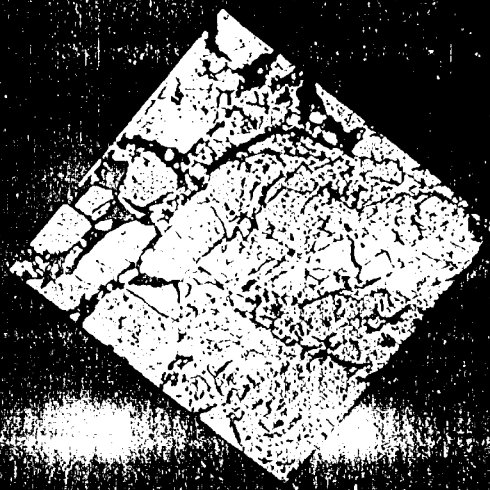
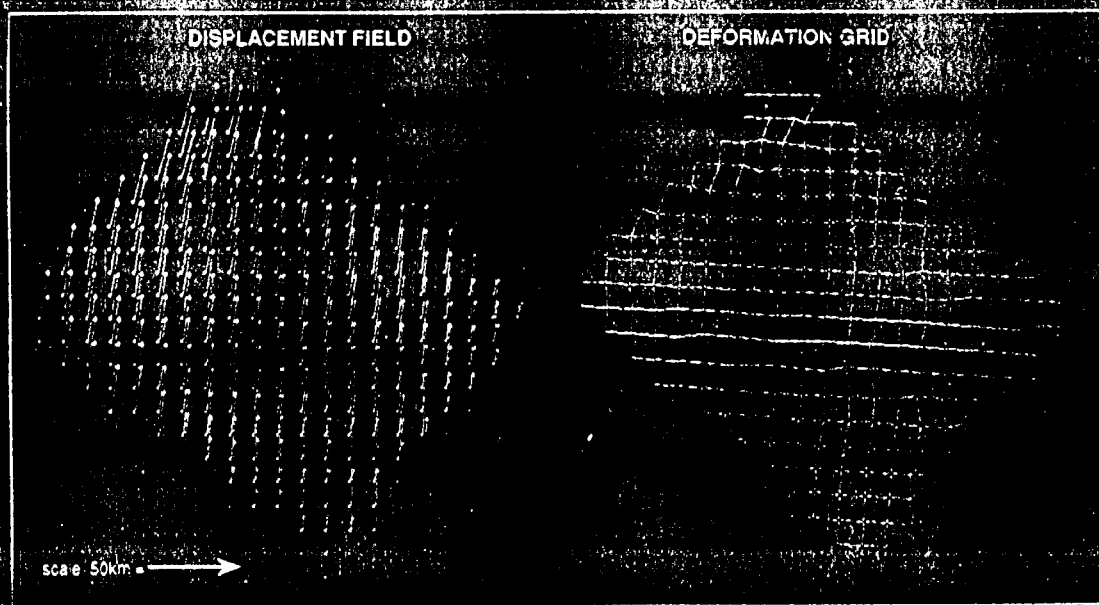
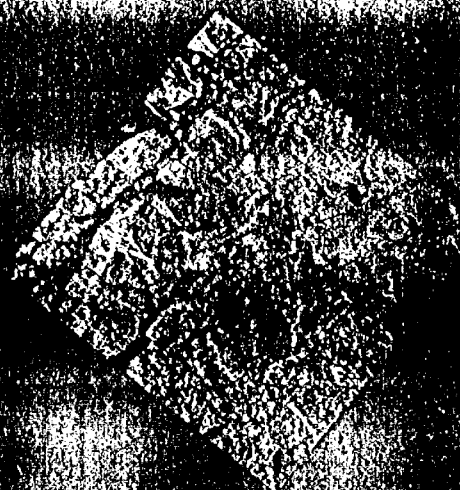
Radarsat Arctic Summer "Snap-Shot"

ScanSAR (460km) Coverage for Episode 1 of 4 (Orbits 029- 057)



J. Crawford / JPL

(Net SAR on-Time: 90 Minutes !)



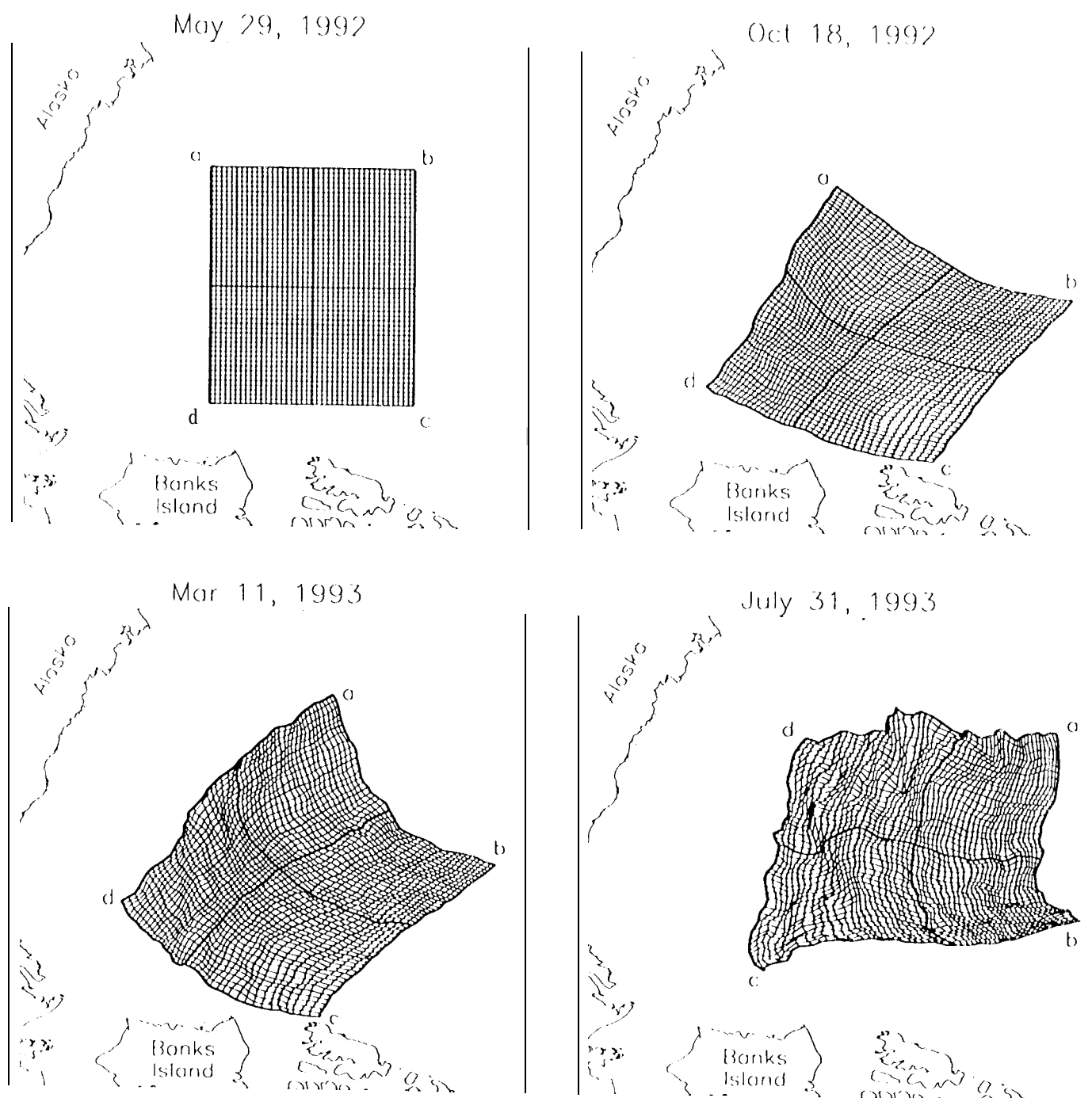


Figure 3. Example showing the deformation of the ice cover over a period from May 1992 through July 1993. Ice age and open water fraction are computed from the area changes of the individual cells.

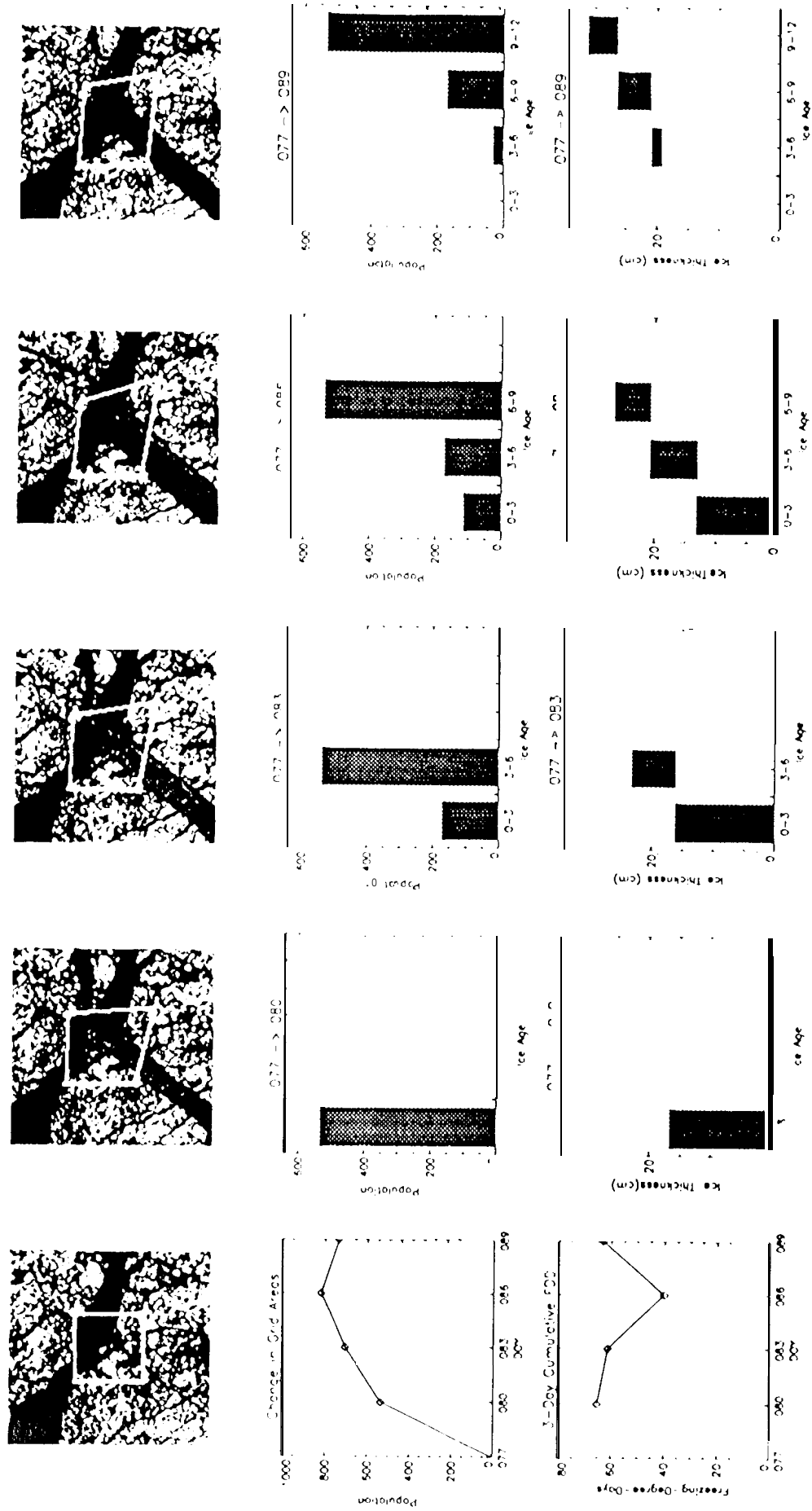
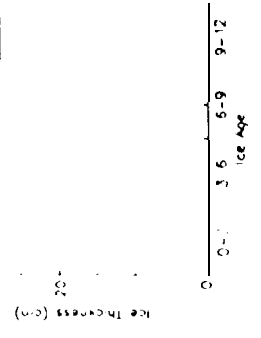
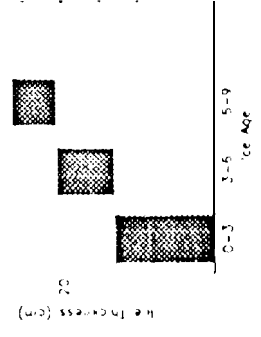
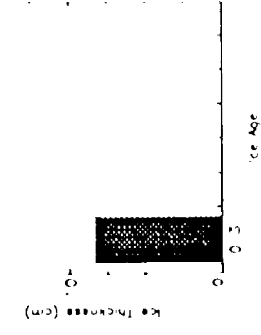
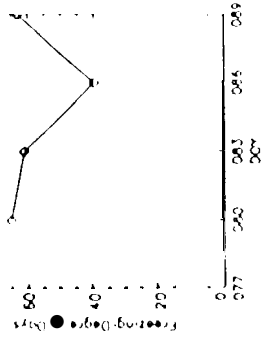
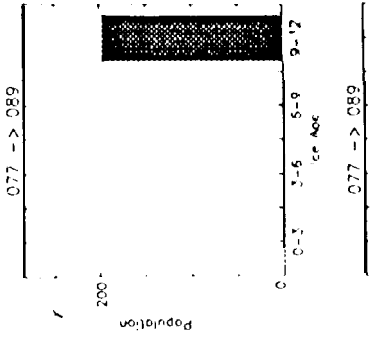
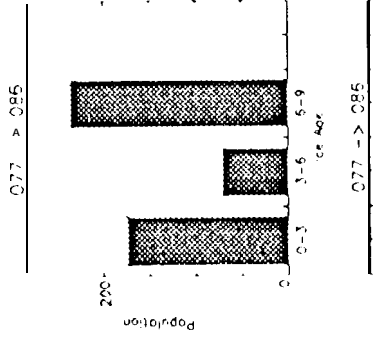
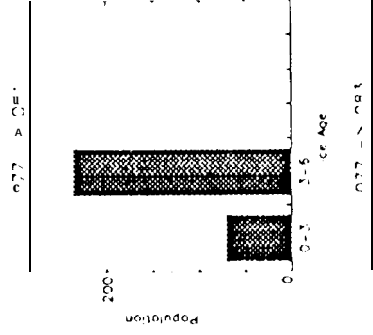
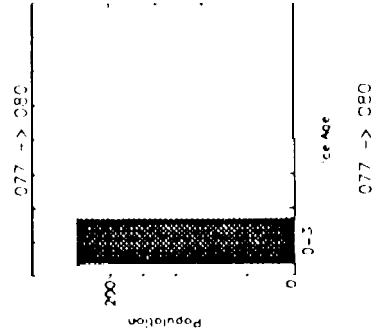
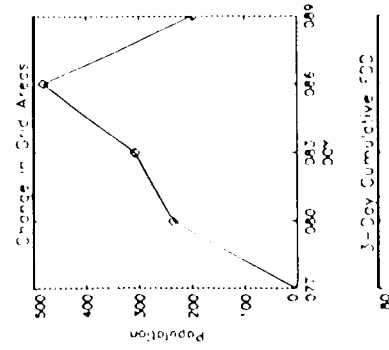
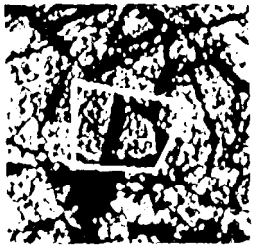
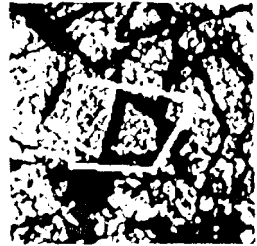
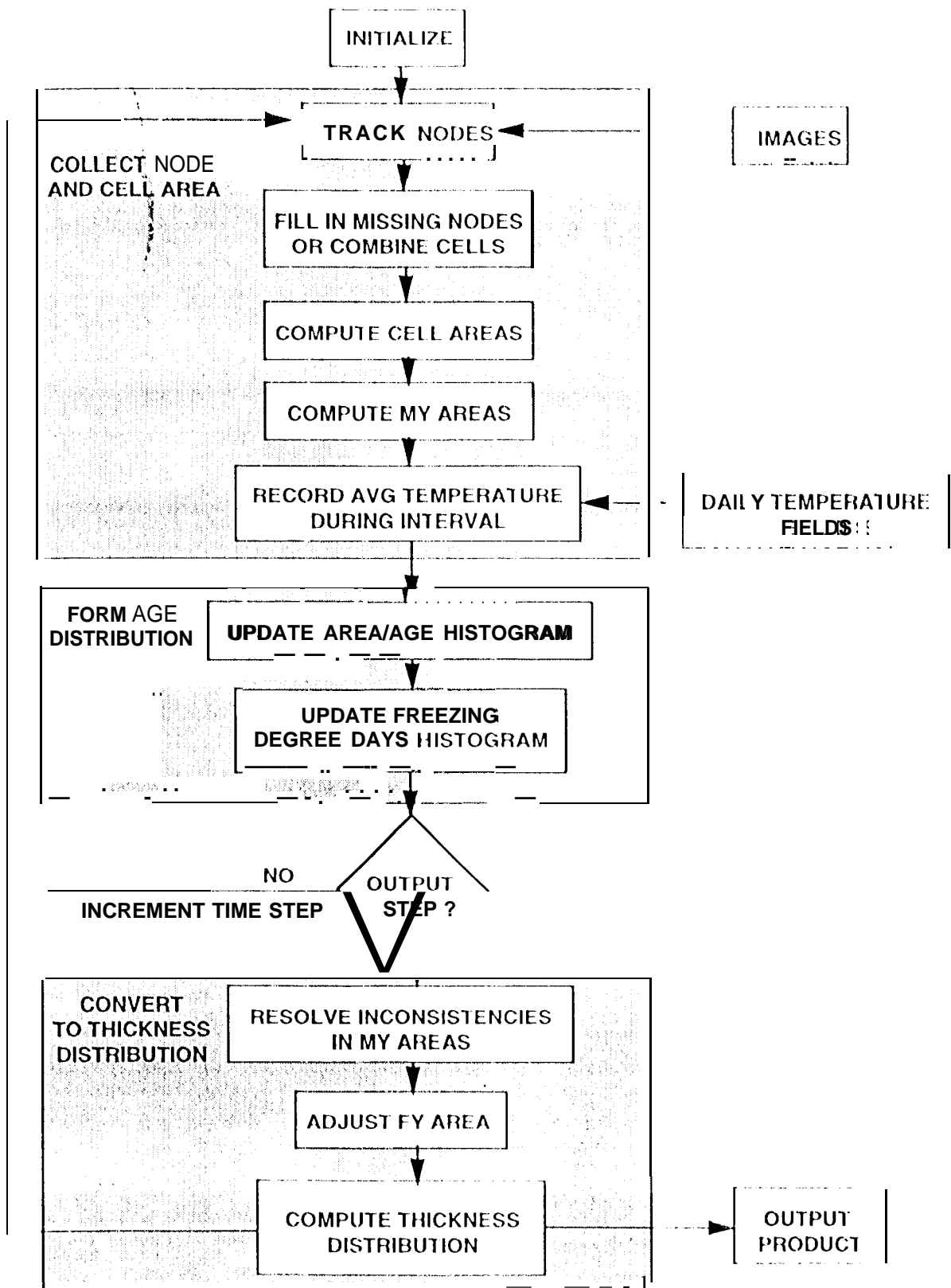
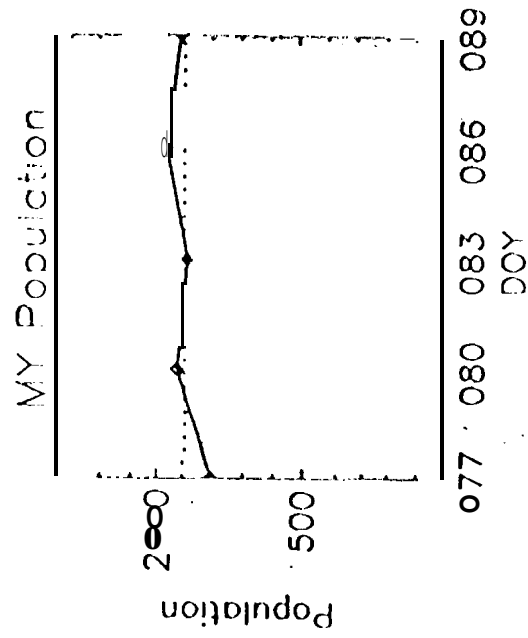
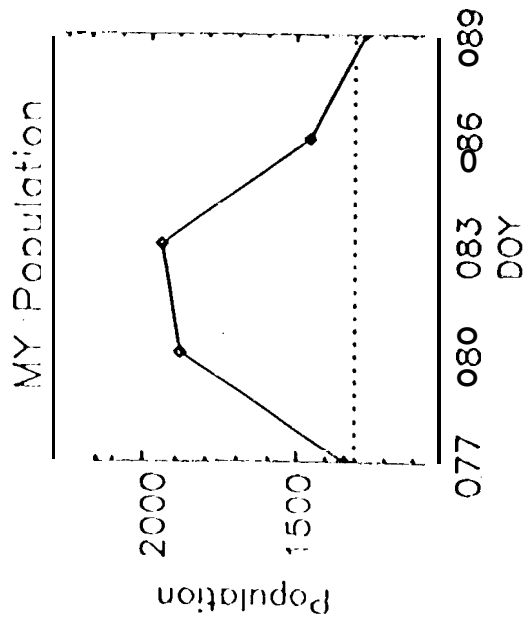
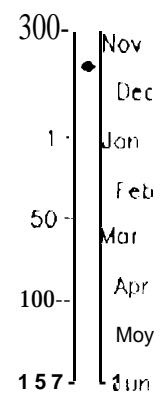
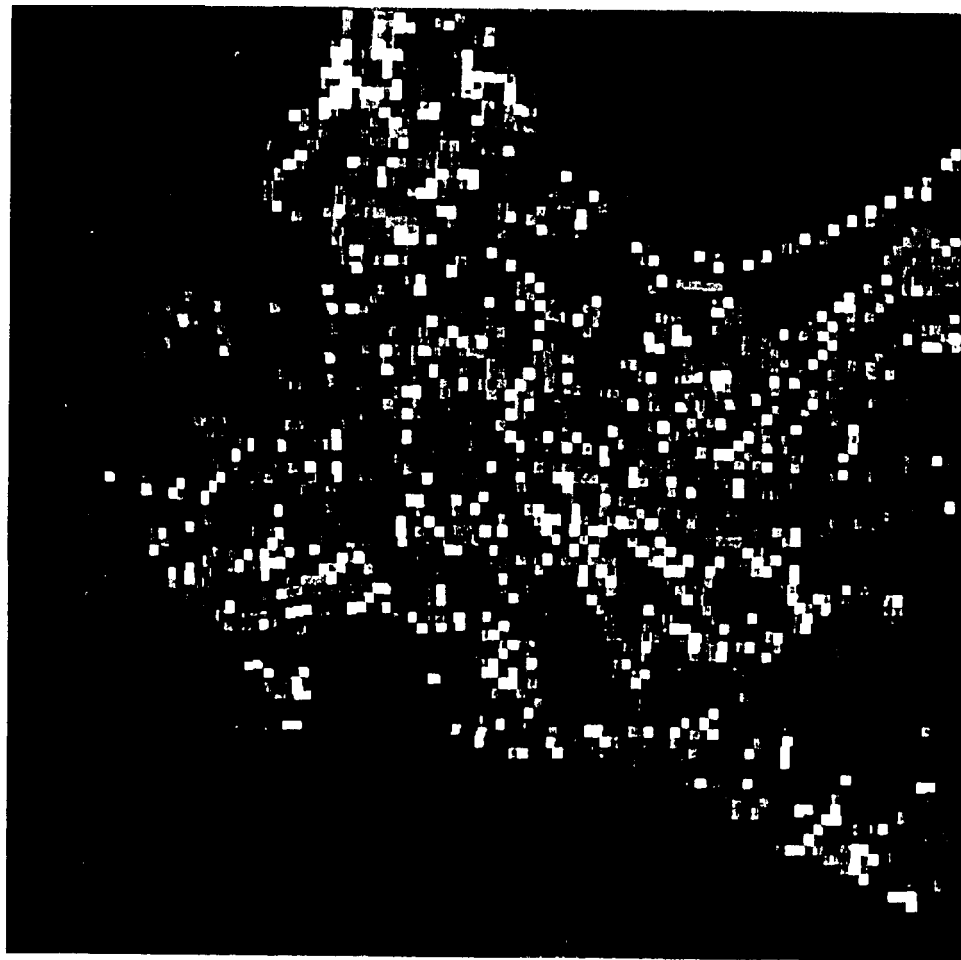


Figure 2. Determination of ice age distribution and thickness distribution in a grid cell extracted from the time sequence (Example 1). (a) The image sequence showing the deformation of a grid cell. (b) Plot of area changes as a function of time, and age histograms computed from the area changes. (c) Plot of the freezing-degree days and the computed thickness of the ice. ($1 \text{ pixel} = 100m \times 100m = 10000 \text{ m}^2 = \text{unit area}$)









Thin ice (%)



